OXFORD

ORIGINAL ARTICLE

A Major Human White Matter Pathway Between Dorsal and Ventral Visual Cortex

Hiromasa Takemura[1], Ariel Rokem[1], Jonathan Winawer[2], Jason D. Yeatman[1,3], Brian A. Wandell[1], and Franco Pestilli[1,4]

[1]Department of Psychology, Stanford University, Stanford, CA, USA, [2]Department of Psychology, New York University, New York, NY, USA, [3]Institute for Learning and Brain Science (ILABS), University of Washington, Seattle, WA, USA, and [4]Department of Psychological and Brain Sciences, Programs in Neuroscience and Cognitive Science, Indiana University, Bloomington, IN, USA

Address correspondence to email: htakemur@stanford.edu (H.T.); franpest@indiana.edu (F.P.)

Abstract

Human visual cortex comprises many visual field maps organized into clusters. A standard organization separates visual maps into 2 distinct clusters within ventral and dorsal cortex. We combined fMRI, diffusion MRI, and fiber tractography to identify a major white matter pathway, the vertical occipital fasciculus (VOF), connecting maps within the dorsal and ventral visual cortex. We use a model-based method to assess the statistical evidence supporting several aspects of the VOF wiring pattern. There is strong evidence supporting the hypothesis that dorsal and ventral visual maps communicate through the VOF. The cortical projection zones of the VOF suggest that human ventral (hV4/VO-1) and dorsal (V3A/B) maps exchange substantial information. The VOF appears to be crucial for transmitting signals between regions that encode object properties including form, identity, and color and regions that map spatial information.

Key words: diffusion-weighted MRI, fiber tractography, vertical occipital fasciculus, visual cortex, white matter

Introduction

Over the last several decades, visual neuroscientists have learned how to use fMRI to identify multiple visual field maps (Fig. 1) in the living human brain (DeYoe et al. 1994; Engel et al. 1994, 1997; Sereno et al. 1995; Wandell et al. 2007; Silver and Kastner 2009; Wandell and Winawer 2011). Several theories have been proposed to characterize the organization of these visual field maps (Wandell et al. 2007). A key theory with substantial support distinguishes between maps located relatively dorsal and those located relatively ventral (Ungerleider and Mishkin 1982; Goodale and Milner 1992; Kravitz et al. 2013).

According to this theory, the ventral stream is mainly engaged in interpreting the properties of color, form, and objects. For example, several lateral and ventral visual field maps in humans (Fig. 1B) have clear stimulus selectivity, such as color selective response in hV4 (Zeki et al. 1991; McKeefry and Zeki 1997; Bartels and Zeki 2000; Wade et al. 2002, 2008; Winawer et al. 2010; Goddard et al. 2011) and shape selective responses in the lateral occipital (LO) areas (Malach et al. 1995; Grill-Spector et al. 2001; Larsson and Heeger 2006; Amano et al. 2009). The dorsal stream is engaged in interpreting spatial organization and guiding action, and dorsal maps in humans (Fig. 1A) have selectivity for motion and disparity (Tootell et al. 1997; Tsao et al. 2003; McKeefry et al. 2008) and spatial attention (Tootell et al. 1998; Schluppeck et al. 2005; Silver et al. 2005; Swisher et al. 2007; Silver and Kastner 2009).

Whereas responses to stimuli in the 2 streams differ (Ungerleider and Mishkin 1982; Goodale and Milner 1992), there are also examples showing relationships between responses measured in these 2 streams (Grill-Spector et al. 1998, 2000; James et al.
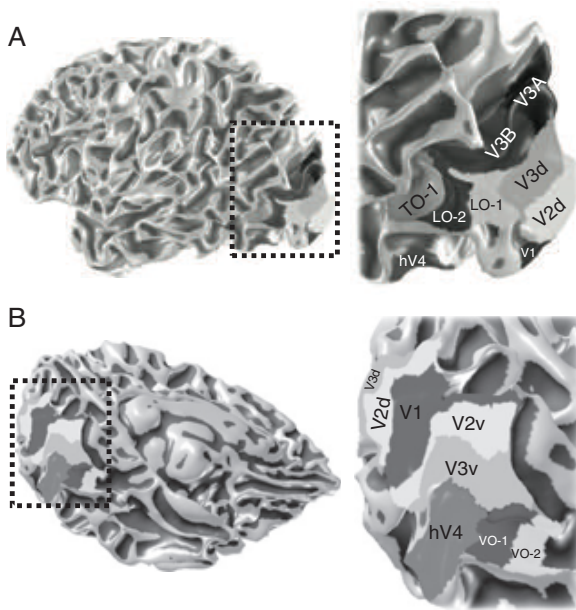
Figure 1. The human dorsal and ventral visual field maps. (A) Lateral view of dorsal visual field maps. (B) Medial view of ventral visual field maps. Rectangular outlines in the left panels indicate the region magnified in right panel. LO, lateral occipital; TO, temporal occipital; VO, ventral occipital (Brewer et al. 2005; Larsson and Heeger 2006; Amano et al. 2009).

2002; Kriegeskorte et al. 2003; Fang and He 2005; Tolias et al. 2005; Konen and Kastner 2008). It seems quite likely that long-range white matter projections must carry the information that communicates between at least some of the maps in these 2 streams.

This study defines the anatomical location and cortical projections of the only known candidate white matter pathway for connecting occipital dorsal and ventral streams. This pathway, the vertical occipital fasciculus (VOF; Wernicke 1881; Yeatman et al. 2013), is little discussed in the vision and cognitive neuroscience literature (Yeatman, Weiner et al. 2014), yet it may be the crucial pathway transmitting signals between these 2 important streams. Finally, we identify a key role for visual hemifield maps V3A/B and hV4/VO-1 which are the principal cortical projection zones of this pathway.

Materials and Methods

MR Data Acquisition and Preprocessing

Subjects
Diffusion-weighted magnetic resonance imaging (DWI) data were collected at Stanford's Center for Cognitive and Neurobiological Imaging (http://cni.stanford.edu/). Five human subjects with normal or corrected-to-normal visual acuity participated in the study (5 males; age range 27–40, mean age 32.6 years old). All subjects participated in 1 scanning session to obtain a high-resolution T_1-weighted anatomical volume, 1–3 functional MRI sessions to measure visual field maps, and 1 diffusion MRI session to measure high-spatial and high-angular resolution diffusion MRI (HARDI) data. Informed written consent was obtained from all subjects. The experimental procedures were approved by the Stanford University Institutional Review Board. The diffusion dataset was used in other publications (Pestilli et al. 2014; Rokem et al. 2015).

Diffusion Data
A dual-spin echo diffusion-weighted sequence (Reese et al. 2003) was used. In each scan, MR images were acquired for 96 different directions of diffusion weighting. The spatial resolution of the measurement was $1.5 \times 1.5 \times 1.5$ mm. The b-value was set to 2000 s/mm^2 and TE was 96.8 ms. Ten nondiffusion-weighted images ($b = 0$) were acquired at the beginning of each scan. Two scans were performed.

MR images were motion corrected to the average $b = 0$ image in each scan, using a rigid body alignment algorithm, implemented in SPM (Friston and Ashburner 2004). The direction of the diffusion gradient in each diffusion-weighted volume was corrected using the rotation parameters from the motion correction procedure. Because of the relatively long duration between the RF excitation and image acquisition in the dual-spin echo sequence used, there is sufficient time for eddy currents to subside. Hence, eddy current correction was not applied. All preprocessing steps have been implemented in Matlab as part of the mrVista software distribution (https://github.com/vistalab/vistasoft).

For *post hoc* correction of EPI spatial distortion, measurements of the B$_0$ magnetic field were performed to DWI data. Field maps were collected in the same slices as the functional data using a 16-shot, gradient echo spiral trajectory pulse sequence. Two volumes were successively acquired, one with TE set to 9.091 ms and one with TE increased by 2.272 ms, and the phase difference between the volumes was used as an estimate of the magnetic field. To track slow drifts in the magnetic field (e.g., due to gradient heating), field maps were collected before and after the diffusion runs as well as periodically between diffusion runs.

Anatomical MRI Acquisition and Tissue Segmentation
The white and gray matter border was defined using a T_1-weighted FSPGR image ($0.7 \times 0.7 \times 0.7$ mm in 4 subjects and $1 \times 1 \times 1$ mm in 1 subject). White/gray matter tissue contrast was increased by averaging 4 T_1 measurements acquired in the same scan session. An initial segmentation was performed using an automated procedure in Freesurfer (Fischl 2012) and refined manually (Yushkevich et al. 2006) (http://www.itksnap.org/pmwiki/pmwiki.php).

Functional Data and Visual Field Maps Estimation
The visual field maps in each hemisphere were identified using the population receptive field (pRF) modeling for fMRI data (Dumoulin and Wandell 2008). Subjects participated in at least 4 fMRI scans (TR; 1.5 s; voxel size; 2.5 mm isotropic in 4 subjects and $2.5 \times 2.5 \times 3$ mm in 1 subject). Stimulus design and analysis methods were the same as the bar scans used in previous studies (Dumoulin and Wandell 2008; Amano et al. 2009; Winawer et al. 2010).

Retinotopic maps were created by projecting the pRF estimates onto cortical surfaces. The borders between most visual areas (V1, V2, V3, V3A/B, hV4, VO-1, VO-2, LO-1, and LO-2) were marked manually at the reversals in polar angles. The borders between hV4 and VO-1 are determined by an eccentricity reversal (Brewer et al. 2005) and an anatomical landmark (Witthoft et al. 2014). VO-2 was not identified in 2 of 10 hemispheres. Maps V3A and V3B were combined in the main analyses, because we could identify the boundary between these maps in only 8 of 10 hemispheres. We performed 1 additional analysis separating V3A and V3B in these 8 hemispheres.

Selection and Validation of White matter Connectomes

We used probabilistic tractography to generate candidate connectome of the human occipital lobe (Tournier et al. 2012). We

used Linear Fascicle Evaluation (LiFE; Pestilli et al. 2014) to optimize these connectomes by eliminating false alarm fascicles and establish the strength of evidence for specific tracts. The LiFE software is available at: http://francopestilli.github.io/life.

Candidate Connectomes Generation

Fiber tracking was performed using MRtrix (Tournier et al. 2012). Diffusion-weighted images were motion-compensated and aligned to the high-resolution T_1-weighted anatomical image. Half of the diffusion data was used for fiber tractography, and the other half was used for cross-validation (see below).

The white matter volume was used as seed region for fiber tracking. The white matter of the occipital lobe was identified from the tissue-type segmentation (see above) and resampled at the resolution of the diffusion data. We used constrained spherical deconvolution (CSD; Tournier et al. 2007) and probabilistic tractography (step size: 0.2 mm; maximum length: 200 mm; minimum length: 10 mm; FOD amplitude cutoff: 0.1) to generate connectomes filling up the occipital white matter. We tested the robustness of the neurobiological results to the choice of analysis parameters by repeating all analyses with different tractography settings. To do so, we tested a range of tracking parameters as implemented MRtrix (minimum radius of curvature: 0.25, 0.5, 1, and 2 mm). The maximum number of harmonics order for the CSD model was also parametrically varied (L_{max} = 2, 4, 6, 8, and 10). This parameter determines the maximum number of deconvolution kernels utilized to estimate the fiber orientation distribution function (fODF) in each voxel by the CSD model. Fiber tracking was performed only within the occipital white matter volume. To identify the candidate connectomes, for each parameter set and brain, we created 3 whole-brain connectomes with 500 000 fascicles (streamlines). We then selected the fascicles located within the occipital white matter for all subsequent analyses (~72 000 fascicles per hemisphere).

Connectome Optimization

Using LiFE, we optimized the candidate connectomes. The general idea of the method is to estimate how much each fascicle in the candidate connectome contributes towards predicting the diffusion signal. This amount is the fascicle weight. We then eliminate fascicles with zero weight to create the optimized connectome (Pestilli et al. 2014). About 17 000 of 72 000 fascicles per hemisphere survive the optimization process. The optimized connectome was used for subsequent analyses.

Virtual Lesion: Statistical Inference on White Matter Tracts

We used a virtual lesion method (Honey and Sporns 2008; Pestilli et al. 2014) to characterize the strength of evidence supporting the VOF. We generated "lesioned" connectome model by excluding the VOF from the optimized connectome. We compared the prediction accuracy (root mean squared error; RMSE) of lesioned model with that of optimized connectome ("unlesioned" model) to evaluate the strength of statistical evidence supporting the existence of the VOF.

We calculated RMSE of 2 models in voxels along the VOF and its path neighborhood (Wedeen et al. 2012; Pestilli et al. 2014). We computed the strength of evidence (S; Pestilli et al. 2014) as the distance between the mean RMSE of the 2 connectomes:

$$S = \frac{\mu_F - \mu_{F'}}{\sqrt{\sigma_F^2 + \sigma_{F'}^2}}. \tag{1}$$

The values μ_F and $\mu_{F'}$ are the bootstrapped means of the RMSE for the lesioned (F) and unlesioned (F') connectome models, respectively. σ_F^2 and $\sigma_{F'}^2$ are the variances of the bootstrapped distributions of mean RMSE for the lesioned (F) and unlesioned (F') connectome models, respectively.

VOF Identification

The VOF is immediately lateral to the ILF, and the core portion of the VOF can be identified based on its superior–inferior principal diffusion direction (PDD; Pajevic and Pierpaoli 1999; Wakana et al. 2004; Yeatman et al. 2013). However, VOF fibers are intermingled with neighboring fasciculi, and tractography based on a model that accounts for crossing fibers (e.g., CSD) is required to reconstruct the full pathway. We segmented the posterior portion of VOF from the optimized connectome in each individual hemisphere by using waypoint ROIs (Catani et al. 2002; Hua et al. 2008; Zhang et al. 2008). The VOF was identified as the set of fascicles passing through 2 axial waypoint plane ROIs, located 3 and 14 mm above the dorsal edge of hV4 (See Supplementary Fig. 1). These planes are located at about $z = -5.8$ and 5, respectively, in ACPC coordinates ($z = -2.7$ and 8.8 in MNI coordinates, respectively). To focus on the posterior portion of the VOF, the waypoints ROIs were limited to $y = -59.2$ in ACPC coordinates anteriorly ($y = -54.3$ in MNI coordinate). ROIs are available for download at http://purl.stanford.edu/bb060nk0241.

Utilizing these waypoints ROIs, we identified a large inhomogeneous fiber bundle containing more than the VOF. The core of the VOF was identified by eliminating fibers classified as outliers for direction, length, and position. To do so, we 1) calculated each fiber's direction in the white matter portion between 2 waypoint ROIs and removed fibers whose direction deviated more than 2 SD from the mean VOF direction, 2) removed fibers with a length ≥3 SD above mean VOF fiber length, and 3) removed fibers with position ≥3 SD away from the mean position of the VOF (Yeatman, Dougherty, Myall et al. 2012). The second and third steps were repeated recursively 3 times. Visualization of the tracts was performed using the Matlab Brain Anatomy toolbox (https://github.com/francopestilli/mba).

Cortical Projection of the VOF

We combined the functionally defined cortical visual field map with the VOF terminations to identify the cortical projection zones of the VOF and their relation to the visual field representations. To identify the cortical projection zones of the VOF, we collected the X, Y, and Z coordinates of the termination of all the VOF fibers. We extended these terminations into the cortical gray matter by applying a 3-dimensional Gaussian smoothing and summing the X, Y, and Z coordinates of fibers terminating within the same cortical voxel. We repeated this process 3 times by using 3 different optimized connectomes (see above) and then averaged. We plotted the normalized projection density on the smoothed cortical surface (see Figs 3A and 4A).

We also measured the coverage of VOF projection at each visual field map. The coverage is defined as the proportion of gray matter voxels in each map within a close distance to the VOF terminations. The coverage is computed 3 times, with different optimized connectomes in each hemisphere, and the results were then averaged. We further repeated this procedure by utilizing 3 distances (1.5, 3, or 4.5 mm in volumetric space) to relate the VOF terminations and the cortical ROIs. We considered distances up to several millimeter to allow for small errors in mapping the

locations of the ROI boundaries and fiber terminations, the latter of which may be subject to small systematic biases such as a tendency to terminate in sulci rather than gyri (Fig. 4A). Figures 3B and 4B describe the proportion of each map covered by the VOF. Results are averaged across all 10 hemispheres.

We compared the VOF projection across optimized connectomes generated using different parameters within optimal range (L_{max} = 4, 6, 8, and 10; the minimum radius of curvature = 0.5 and 1 mm). We utilized 3 mm distance to define a cortical projection of VOF in each optimized connectome. Supplementary Figures 7, 8, 13, and 14 describe the comparison of VOF coverage across different connectome models.

Results

The existence of the VOF was established by classical and recent post-mortem fiber dissection studies (Martino and Garcia-Porrero 2013; see Yeatman, Weiner et al. 2014 for a review on classical studies). But the relationship between the VOF cortical projection zones and early visual field maps was unknown. Here, we used diffusion MRI and fiber tractography to identify the posterior portion of the VOF in 10 hemispheres (see Supplementary Materials and Methods). We then assessed the strength of the statistical evidence supporting the existence of the VOF given the measured diffusion signal (Pestilli et al. 2014). Finally, we used fMRI to characterize the VOF cortical projections with respect to the dorsal and ventral visual field maps.

VOF Identification and Statistical Evaluation

Figure 2A shows the VOF identified in 1 representative hemisphere (see Supplementary Materials and Methods, and Supplementary Fig. 2). The VOF projects to both the dorsal part of occipital cortex and the lateral portion of ventral occipital cortex. The VOF is located posterior to the arcuate fasciculus (Martino and Garcia-Porrero 2013) and lateral to the optic radiation (Fig. 2A). We identified the VOF in 10 hemispheres (Fig. 2B) in a consistent position relative to the posterior segment of the arcuate fasciculus and the optic radiation. The mean VOF length is 3.7 cm (SD = 0.3 cm, N = 10) and its volume is 2.3 mL (SD = 0.5 mL, N = 10). The range of sizes is similar to that observed in the surface area of visual field maps (Dougherty et al. 2003). The VOF location can be inferred from the PDD map generated by a diffusion tensor fit (Pajevic and Pierpaoli 1999; Wakana et al. 2004; Yeatman et al. 2013). Supplementary Figure 3 shows the location of the posterior portion of the VOF identified using tractography (Tournier et al. 2012; Pestilli et al. 2014) and projected on the PDD of representative brain slices. The VOF location is blue, indicating a primarily vertical (superior–inferior) PDD. Supplementary Figure 4 also shows the location of VOF identified from a PDD map in Human Connectome Project dataset (Van Essen et al. 2013).

We used the LiFE algorithm (Pestilli et al. 2014; see Supplementary Materials and Methods and Supplementary Fig. 2) to establish the strength of evidence in favor of the VOF. The LiFE algorithm treats a connectome (the complete set of white matter tracts and connections in a brain volume; Sporns et al. 2005; Hagmann et al. 2010) as a model of the measured diffusion signal. LiFE uses the connectome model to generate synthetic diffusion signals. While generating synthetic diffusion signal, LiFE eliminates fascicles that do not contribute to the diffusion prediction (false alarm fascicles; Pestilli et al. 2014). The RMSE between the

synthetic and the measured signal measures the accuracy of the connectome model. The connectome without false alarm fascicles is called the optimized connectome.

We used LiFE to compute the accuracy of several optimized connectome models; each was constructed using different tractography (minimum radius of curvature; Tournier et al. 2012) and constrained spherical deconvolution parameters (L_{max}; see Supplementary Materials and Methods; Tournier et al. 2007, 2012). The accuracy of the optimized connectome derived using the recommended parameters (L_{max} = 8; minimum radius of curvature = 1 mm; Tournier et al. 2012) was equal or better than other choices (see Supplementary Figs 5 and 6; also Supplemental Materials and Methods). All subsequent analyses were performed using the recommended parameters.

Finally, we used LiFE to evaluate the strength of evidence (S; Pestilli et al. 2014) supporting the existence of the VOF. S is computed by removing the VOF from the optimized connectome and recalculating the prediction error (see Virtual lesion in Supplementary Materials and Methods). The mean strength of evidence is S = 28.89 (28.98, 29.80, 41.33, 27.55, and 19.68 for left hemispheres; 29.91, 32.81, 31.85, 30.11, and 16.90 for right hemispheres). Supplementary Figure 9 shows the comparison of the S on the VOF and other major fascicles reported in a previous study (Pestilli et al. 2014). The evidence on the VOF is smaller than several major fascicles (SLF, ILF, and Arcuate) but comparable with relatively smaller fascicles (e.g., Uncinate). Hence, there is visible evidence (see Supplementary Figs 3 and 4) and very strong statistical evidence supporting the existence of the VOF in the human brain.

Dorsal VOF Projections

Next, we established the dorsal and ventral visual field maps containing the VOF cortical projections. The visual field map boundaries and pRFs were measured using fMRI (see Supplementary Materials and Methods; Dumoulin and Wandell 2008). Figure 3A shows the cortical projection areas of the posterior portion of the VOF on the dorsal cortical surface of 2 hemispheres.

Figure 3B describes the proportion of the voxels in each map that are within a specific distance (1.5, 3, and 4.5 mm) of a dorsal VOF termination. There is a major dorsal VOF projection to V3A/B. Across all hemispheres, the majority of VOF terminations are within 4 mm of V3A/B. We frequently observe projections to neighboring V3d as well. Across 10 hemispheres, 82.0% of these posterior VOF dorsal cortical projections terminate near V3A/B or V3d, but they are rarely near V2d, V1, or the intraparietal sulcus (IPS) maps. The anterior portion of the VOF contains additional projection zones in more anterior dorsal and ventral cortex. These results are robust to the choice of diffusion model and tractography parameters (see Supplementary Figs 7 and 8).

Strong Evidence Supporting VOF Projections to V3A/B
To test the strength of the evidence supporting the VOF projections to V3A/B, we compared the connectome prediction error with the VOF fascicles projecting to V3A/B removed (lesioned connectome) or not (unlesioned connectome). The prediction error is substantially higher when these fascicles are removed. The mean strength of the evidence (S) for the VOF projections to V3A/B is 25.72 (see Supplementary Fig. 10).

We repeated the analysis for V3d and V2d. Evidence for VOF projections for V3d is lower, S = 15.34 and is small for V2d (mean S = 6.53; see Supplementary Fig. 10). The data strongly
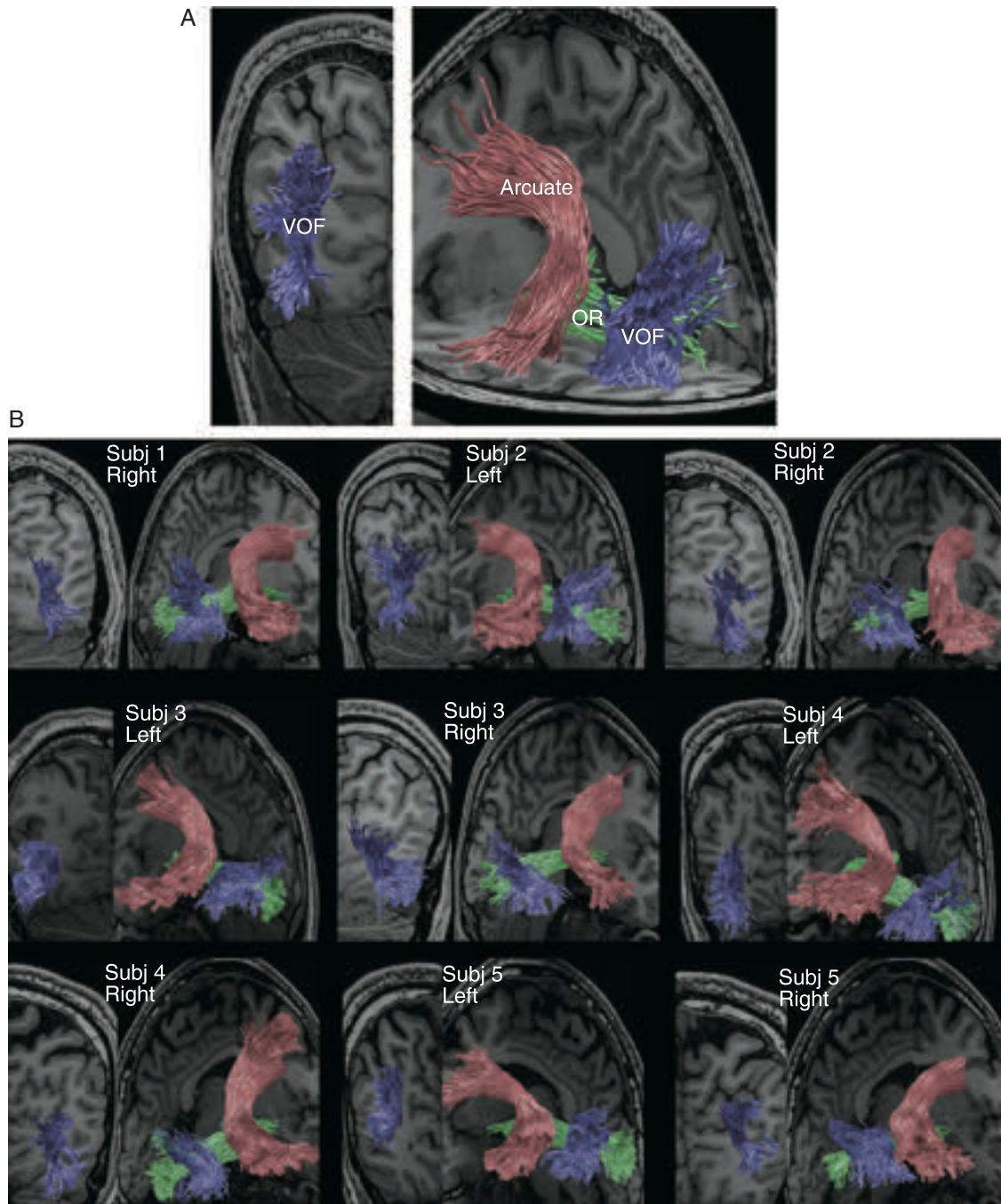
Figure 2. Identification of the human VOF. (*A*) Left, coronal view of the VOF in 1 living brain (blue, Subject 1, left hemisphere). Right, VOF trajectory within the occipital lobe in relation to the arcuate fasciculus (red, more anterior) and the optic radiation (OR, green, medial). (*B*) The VOF identified from other 9 hemispheres.

support the VOF projections to V3A/B. There is some evidence for the VOF projections to V3d and smaller evidence for V2d.

Dorsal VOF Projections Are Uniformly Distributed Between V3A and V3B

We managed to subdivide maps V3A and V3B in 8 out of 10 hemispheres. The VOF projects to large portions of both V3A and V3B (see Supplementary Fig. 11). The strength of the evidence is comparable for V3A and V3B (see Supplementary Fig. 12; V3A, mean $S = 23.40$; V3B, mean $S = 21.29$), suggesting that VOF projections are present in both V3A and V3B.

Ventral VOF Projections

We analyzed the VOF cortical projection areas in relation to visual field maps in the posterior occipital ventral stream (Fig. 4A). There are VOF projections to hV4 in all 10 hemispheres, so that the majority of hV4 voxels are within 4 mm of VOF terminations (Fig. 4B). There are limited projections to V3v, mostly restricted to the lateral portion of the map, representing foveal visual field (Fig. 4A). Very few fascicles project to V2v. The VOF also terminates near other ventral maps such as VO-1 (Brewer et al. 2005), and lateral maps such as LO-1 and LO-2 (Larsson and Heeger 2006; Amano et al. 2009; Silson et al. 2013). However, the map
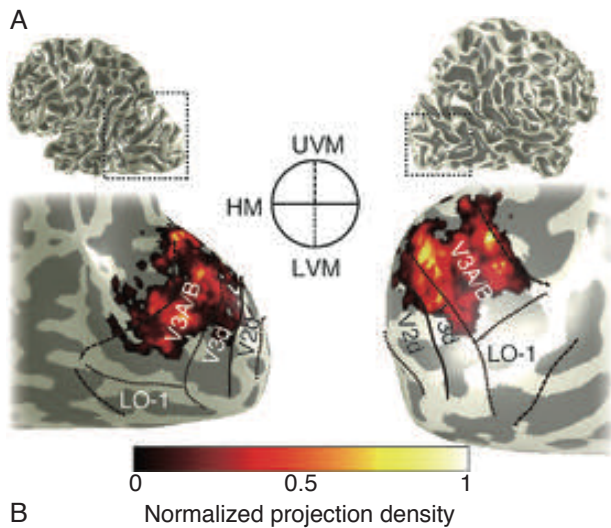
Figure 3. VOF cortical projections in the dorsal visual field maps. (A) Projection pattern of VOF plotted on the cortical surface (Left panel; Subject 1, left hemisphere; Right panel; Subject 4, right hemisphere). The small image on the top indicates the region shown in magnified and smoothed form on the bottom. Color map depicts a normalized VOF projection density. Visual field map boundaries were identified using the pRF method and are reported as line segments corresponding to polar angle reversals (circular inset; UVF, upper vertical meridian; HM, horizontal meridian; LVM, lower vertical meridian; see caption at the center). (B) VOF map coverage averaged across 10 hemispheres. Vertical axis represents the proportion of voxels in maps within 1.5 mm (blue), 3 mm (green), and 4.5 mm (red) from dorsal VOF terminations. Error bar depicts ±1 SEM across hemispheres. See Supplementary Figure 7, 8, 10–12 for additional analyses.

Figure 4. VOF cortical projections in the ventral visual field maps. (A) Ventral VOF projection covers hV4, VO-1, LO-map, and the regions between hV4 and LO-map (Left panel; Subject 1, left hemisphere; Right panel; Subject 4, right hemisphere). Figure captions are identical to those in Figure 3 except the green line depicting the eccentricity reversals between hV4 and VO-1 (Brewer et al. 2005; Witthoft et al. 2014). (B) VOF map coverage in each visual field map averaged across 10 hemispheres. Vertical axis represents the proportion of voxels in maps within 1.5 mm (blue), 3 mm (green), and 4.5 mm (red) from dorsal VOF terminations. Left panel, projection in ventral visual field maps. Right panel, projections in LO maps. Error bar depicts ±1 SEM across hemispheres. See Supplementary Figures 13–15 for additional analyses.

coverage in these regions is much lower than the hV4 map coverage (Fig. 4B). The results are consistent across a range of diffusion model and tractography parameters (see Supplementary Figs 13 and 14).

In addition, the VOF has large projections into cortical regions with difficult visual field maps assignment due to their predominantly foveal representation and to the existence of MRI artifacts (No Man's Land; Winawer et al. 2010). These projections are likely to include the phPIT region (Kolster et al. 2010) and one of the face selective patches (IOG-faces; Weiner and Grill-Spector 2010). The ventral VOF projections are also likely to extend to regions anterior to VO-1 including the visual word form area (VWFA; Cohen et al. 2000, 2002; Ben-Shachar et al. 2007; Yeatman et al. 2013).

Strength of Evidence Supporting VOF Projections into hV4
To test the strength of the evidence supporting VOF projections to hV4, we compared the connectome prediction error with and

without the VOF fascicles projecting to hV4 (virtual lesion). There is reliable evidence for VOF projections to hV4 (S = 16.68; see Supplementary Fig. 15) and some evidence for VO-1 (S = 11.58; see Supplementary Fig. 15). The strength of evidence for VOF projections to V3v, LO-1, and LO-2 is smaller than for hV4 (S = 9.59, 8.47, and 9.18, respectively; see Supplementary Fig. 15). The strength of evidence is small for V2v (S = 5.04; see Supplementary Fig. 15). The analyses support a projection pattern in which the principal VOF terminations are near hV4 and perhaps VO-1.

Stronger Evidence for VOF Projection to Ventro-lateral Than Ventro-medial Cortex
Early visual areas, such as V1, V2, and V3, are located on the medial surface of the occipital lobe. The analysis of the ventral VOF projections suggests that ventral maps on medial surface (V2v and V3v) do not receive major VOF projections (Fig. 4). The visual field maps located on the lateral side instead (hV4, VO-1, and LO-map) receive larger VOF projections.

To test whether the VOF projects primarily to ventro-lateral cortex, we identified the anatomical location of the collateral
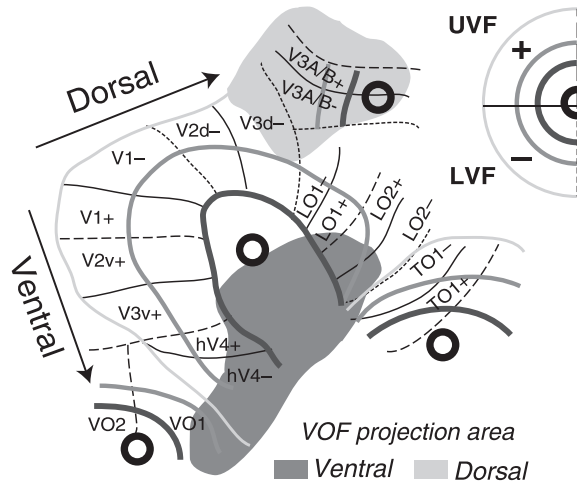
Figure 5. The VOF communication diagram. Schematic diagram of the VOF projections. Visual field topography was described in a flattened format for the right hemisphere (Larsson and Heeger 2006). Gray regions depict the projection zone of VOF (light gray, dorsal; dark gray, ventral).

sulcus (CoS; see Supplementary Fig. 16A and B) in each hemisphere. The CoS separates ventro-lateral from ventro-medial VOF fascicles (see Supplementary Fig. 16C). We then tested the strength of the evidence supporting VOF projections to either side of CoS by computing S for the medial and lateral fascicles. The scatter plot compares the strength of the evidence supporting lateral compared with that for medial-ventral VOF projections (see Supplementary Fig. 16D). The strength of the evidence supporting VOF projections into ventro-lateral cortex is substantially larger than that for ventro-medial projections. Hence, the VOF mainly connects dorsal and ventro-lateral regions.

Discussion

The dorsal and ventral map connections mediated by the VOF are illustrated schematically in Figure 5. Dorsal VOF projections are dense in V3A/B and extend to V3d (green). Ventral VOF projections cover a wide area on the ventral surface, principally on the lateral surface (pink). VOF cortical projections terminate in hV4, VO-1, and LO-1/LO-2 as well as the cortical region between these maps, which has not yet been definitively mapped (No Man's Land; Winawer et al. 2010).

VOF and Visual Field Map Functionality

The anatomy suggests that the VOF carries signals between ventral regions that encode object properties including form, identify, and color information (Zeki et al. 1991; Malach et al. 1995; McKeefry and Zeki 1997; Cohen et al. 2000; Wade et al. 2002, 2008) and dorsal regions that map spatial location to action plans (Tootell et al. 1997; Tsao et al. 2003; Fischer et al. 2012; Merriam et al. 2013).

A number of previous fMRI studies reported concurrent activation in dorsal and ventral regions for particular sets of stimuli as well as a clear similarity between some dorsal and ventral areas in terms of stimulus selectivity. For example, Grill-Spector and colleagues (1998) compared cortical activation for motion-defined form stimuli and moving noise stimuli. They found concurrent activation in dorsal (V3A) and ventral stream (LO) regions for motion-defined stimuli, suggesting that communication between the dorsal and ventral streams plays a role in cue

invariance in object recognition. Complimenting these findings, there are studies showing object-selective responses in dorsal regions (Grill-Spector et al. 2000; James et al. 2002; Fang and He 2005; Konen and Kastner 2008; Vinberg and Grill-Spector 2008). Rokers and colleagues (2009) reported that in addition to hMT+ and V3A, LO also showed selectivity for 3-dimensional motion. Costagli and colleagues (2014) measured the cortical response to increments and decrements of motion coherence, and identified that V3B and hV4 similarly showed positive responses to both increments and decrements. Other lines of studies (Döven-cioğlu et al. 2013; Murphy et al. 2013) demonstrated that V3B is involved in stereo cue integration (disparity, texture, and shade), which could be the outcome of dorsal-ventral communication. A recent study (Saber et al. 2015) showed that saccade planning evokes BOLD activity not only in dorsal (V3A/B, IPS0) but also in ventral visual areas (hV4, VO-1). All of these studies suggest substantial communication between the dorsal and ventral maps. The anatomical description of the VOF makes it the likely pathway to carry signals coordinating dorsal and ventral stream processing.

Comparison Between Human and Macaque

There are many functional and structural differences between visual cortex in human and macaque. For example, concerning the visual field maps, interspecies differences have been identified in the position of V4 (McKeefry and Zeki 1997; Wade et al. 2008; Arcaro et al. 2009; Winawer et al. 2010; Goddard et al. 2011; Witthoft et al. 2014), the volume of V3 (Brewer et al. 2002; Dougherty et al. 2003; Lyon and Connolly 2012), and responses to moving stimuli in V3A (Tootell et al. 1997; Vanduffel et al. 2001). Moreover, there are no certain homologies between the human V3B (Smith et al. 1998; Press et al. 2001) and the LO-maps (Larsson and Heeger 2006; Amano et al. 2009) and macaque maps. All of these maps have been identified as VOF terminations in this study.

Given these significant interspecies differences, it is important to understand white matter tracts and their cortical projection zones in human directly. Identifying the path of the white matter tracts in humans has the added advantage that properties of the tracts can be studied in relation to health, disease, and development (Dougherty et al. 2007; Fields 2008; Thomas et al. 2009; Thiebaut de Schotten et al. 2011; Thomason and Thompson 2011; Lebel et al. 2012; Wandell et al. 2012; Yeatman, Dougherty, Ben-Shachar et al. 2012; Johnson et al. 2013; Wandell and Yeatman 2013; Ogawa et al. 2014; Tavor et al. 2014; Yeatman, Wandell et al. 2014; Allen et al. 2015; Gomez et al. 2015).

The present study extends post-mortem macaque brain studies (Felleman and Van Essen 1991; Ungerleider et al. 2008) to in vivo methods in the human brain. We have learned that the VOF is a major tract occupying a substantial volume of the occipital white matter. We show that its path and projections can be reliably defined using modern diffusion MRI methods in living brains. This is the first study to characterize the cortical projections of the VOF in relation to the visual field maps.

Early Hubs of Ventro-Dorsal Visual Communication

Primate V2 and V3 have split representations of the contralateral hemifield, with dorsal and ventral regions responding to stimuli in the lower and upper quarterfields, respectively. In humans, the visual field maps adjacent and anterior to V3 are not split: these maps have a full hemifield representation confined within the dorsal (V3A/B) and ventral (hV4 and VO-1) surfaces (Tootell

et al. 1997; Press et al. 2001; Brewer et al. 2005; Arcaro et al. 2009;
Winawer et al. 2010; Goddard et al. 2011; Wandell and Winawer
2011).
Because of their hemifield representation, these maps
are natural candidates for information hubs that communicate
between ventral and dorsal streams. We have shown that the
VOF communicates preferentially between these maps. Future
measurements and models will benefit from mapping the func-
tional responses of these maps in humans and by considering
their potential role as communication hubs between dorsal and
ventral cortex.

Conclusion

Many cognitive activities such as reading this page require fast
and accurate coordination between motor actions (e.g., eye
movements) and object identification (e.g., word recognition;
Vidyasagar and Pammer 2010). The human brain comprises
distinct cortical regions specialized for seeing objects and pro-
cessing spatial information that are separated by several centi-
meters in ventral and dorsal occipital cortex. The anatomy of
the human brain requires a major white matter communication
pathway between the dorsal and ventral streams. The VOF is a
strong candidate for channeling communication between dorsal
and ventral visual streams. Characterizing the VOF in individual,
living human brains provides a new opportunity for understand-
ing how signals pass between dorsal and ventral visual cortex
and to understand the role of these signals in health and disease.

Supplementary Material

Supplementary material can be found at: http://www.cercor.
oxfordjournals.org/.

Funding

Notes

References

Allen B, Spiegel DP, Thompson B, Pestilli F, Rokers B. 2015. Altered
white matter in early visual pathways of human amblyopes.
Vision Res. [Epub ahead of print].

Amano K, Wandell BA, Dumoulin SO. 2009. Visual field maps,
population receptive field sizes, and visual field coverage in
the human MT+ complex. J Neurophysiol. 102:2704–2718.

Arcaro MJ, McMains SA, Singer BD, Kastner S. 2009. Retinotopic
organization of human ventral visual cortex. J Neurosci.
29:10638–10652.

Bartels A, Zeki S. 2000. The architecture of the colour centre in the
human visual brain: new results and a review. Eur J Neurosci.
12:172–193.

Ben-Shachar M, Dougherty RF, Deutsch GK, Wandell BA. 2007.
Differential sensitivity to words and shapes in ventral occipi-
to-temporal cortex. Cereb Cortex. 17:1604–1611.

Brewer AA, Liu J, Wade AR, Wandell BA. 2005. Visual field maps
and stimulus selectivity in human ventral occipital cortex.
Nat Neurosci. 8:1102–1109.

Brewer AA, Press WA, Logothetis NK, Wandell BA. 2002. Visual
areas in macaque cortex measured using functional magnetic
resonance imaging. J Neurosci. 22:10416–10426.

Catani M, Howard RJ, Pajevic S, Jones DK. 2002. Virtual in vivo
interactive dissection of white matter fasciculi in the
human brain. NeuroImage. 17:77–94.

Cohen L, Dehaene S, Naccache L, Lehericy S, Dehaene-
Lambertz G, Henaff MA, Michel F. 2000. The visual word
form area: spatial and temporal characterization of an initial
stage of reading in normal subjects and posterior split-brain
patients. Brain. 123(Pt 2):291–307.

Cohen L, Lehericy S, Chochon F, Lemer C, Rivaud S, Dehaene S.
2002. Language-specific tuning of visual cortex? Functional
properties of the Visual Word Form Area. Brain. 125:
1054–1069.

Costagli M, Ueno K, Sun P, Gardner JL, Wan X, Ricciardi E,
Pietrini P, Tanaka K, Cheng K. 2014. Functional signalers of
changes in visual stimuli: cortical responses to increments
and decrements in motion coherence. Cereb Cortex.
24:110–118.

DeYoe EA, Bandettini P, Neitz J, Miller D, Winans P. 1994. Func-
tional magnetic resonance imaging (FMRI) of the human
brain. J Neurosci Methods. 54:171–187.

Dougherty RF, Ben-Shachar M, Deutsch GK, Hernandez A, Fox GR,
Wandell BA. 2007. Temporal-callosal pathway diffusivity pre-
dicts phonological skills in children. Proc Natl Acad Sci USA.
104:8556–8561.

Dougherty RF, Koch VM, Brewer AA, Fischer B, Modersitzki J,
Wandell BA. 2003. Visual field representations and
locations of visual areas V1/2/3 in human visual cortex. J
Vis. 3:586–598.

Dövencioğlu D, Ban H, Schofield AJ, Welchman AE. 2013. Percep-
tual integration for qualitatively different 3-D cues in the
human brain. J Cogn Neurosci. 25:1527–1541.

Dumoulin SO, Wandell BA. 2008. Population receptive field esti-
mates in human visual cortex. NeuroImage. 39:647–660.

Engel SA, Glover GH, Wandell BA. 1997. Retinotopic organization
in human visual cortex and the spatial precision of functional
MRI. Cereb Cortex. 7:181–192.

Engel SA, Rumelhart DE, Wandell BA, Lee AT, Glover GH,
Chichilnisky EJ, Shadlen MN. 1994. fMRI of human visual cor-
tex. Nature. 369:525.

Fang F, He S. 2005. Cortical responses to invisible objects in the
human dorsal and ventral pathways. Nat Neurosci.
8:1380–1385.

Felleman DJ, Van Essen DC. 1991. Distributed hierarchical pro-
cessing in the primate cerebral cortex. Cereb Cortex. 1:1–47.

Fields RD. 2008. White matter in learning, cognition and psychi-
atric disorders. Trends Neurosci. 31:361–370.

Fischer E, Bulthoff HH, Logothetis NK, Bartels A. 2012. Human
areas V3A and V6 compensate for self-induced planar visual
motion. Neuron. 73:1228–1240.

Fischl B. 2012. FreeSurfer. NeuroImage. 62:774–781.

Friston KJ, Ashburner J. 2004. Generative and recognition models
for neuroanatomy. NeuroImage. 23:21–24.

Goddard E, Mannion DJ, McDonald JS, Solomon SG, Clifford CW. 2011. Color responsiveness argues against a dorsal component of human V4. J Vis. 11(4):3.

Gomez J, Pestilli F, Witthoft N, Golarai G, Liberman A, Poltoratski S, Yoon J, Grill-Spector K. 2015. Functionally defined white matter reveals segregated pathways in human ventral temporal cortex associated with category-specific processing. Neuron. 85:216–227.

Goodale MA, Milner AD. 1992. Separate visual pathways for perception and action. Trends Neurosci. 15:20–25.

Grill-Spector K, Kourtzi Z, Kanwisher N. 2001. The lateral occipital complex and its role in object recognition. Vision Res. 41:1409–1422.

Grill-Spector K, Kushnir T, Edelman S, Itzchak Y, Malach R. 1998. Cue-invariant activation in object-related areas of the human occipital lobe. Neuron. 21:191–202.

Grill-Spector K, Kushnir T, Hendler T, Malach R. 2000. The dynamics of object-selective activation correlate with recognition performance in humans. Nat Neurosci. 3:837–843.

Hagmann P, Cammoun L, Gigandet X, Gerhard S, Grant PE, Wedeen V, Meuli R, Thiran JP, Honey CJ, Sporns O. 2010. MR connectomics: principles and challenges. J Neurosci Methods. 194:34–45.

Honey CJ, Sporns O. 2008. Dynamical consequences of lesions in cortical networks. Hum Brain Mapp. 29:802–809.

Hua K, Zhang J, Wakana S, Jiang H, Li X, Reich DS, Calabresi PA, Pekar JJ, van Zijl PC, Mori S. 2008. Tract probability maps in stereotaxic spaces: analyses of white matter anatomy and tract-specific quantification. NeuroImage. 39:336–347.

James TW, Humphrey GK, Gati JS, Menon RS, Goodale MA. 2002. Differential effects of viewpoint on object-driven activation in dorsal and ventral streams. Neuron. 35:793–801.

Johnson RT, Yeatman JD, Wandell BA, Buonocore MH, Amaral DG, Nordahl CW. 2013. Diffusion properties of major white matter tracts in young, typically developing children. NeuroImage. 88C:143–154.

Kolster H, Peeters R, Orban GA. 2010. The retinotopic organization of the human middle temporal area MT/V5 and its cortical neighbors. J Neurosci. 30:9801–9820.

Konen CS, Kastner S. 2008. Two hierarchically organized neural systems for object information in human visual cortex. Nat Neurosci. 11:224–231.

Kravitz DJ, Saleem KS, Baker CI, Ungerleider LG, Mishkin M. 2013. The ventral visual pathway: an expanded neural framework for the processing of object quality. Trends Cogn Sci. 17:26–49.

Kriegeskorte N, Sorger B, Naumer M, Schwarzbach J, van den Boogert E, Hussy W, Goebel R. 2003. Human cortical object recognition from a visual motion flowfield. J Neurosci. 23:1451–1463.

Larsson J, Heeger DJ. 2006. Two retinotopic visual areas in human lateral occipital cortex. J Neurosci. 26:13128–13142.

Lebel C, Gee M, Camicioli R, Wieler M, Martin W, Beaulieu C. 2012. Diffusion tensor imaging of white matter tract evolution over the lifespan. NeuroImage. 60:340–352.

Lyon DC, Connolly JD. 2012. The case for primate V3. Proc Biol Sci. 279:625–633.

Malach R, Reppas JB, Benson RR, Kwong KK, Jiang H, Kennedy WA, Ledden PJ, Brady TJ, Rosen BR, Tootell RB. 1995. Object-related activity revealed by functional magnetic resonance imaging in human occipital cortex. Proc Natl Acad Sci USA. 92:8135–8139.

Martino J, Garcia-Porrero JA. 2013. In reply: Wernicke's perpendicular fasciculus and vertical portion of the superior longitudinal fasciculus. Neurosurgery. 73(2):E382–E383.

McKeefry DJ, Burton MP, Vakrou C, Barrett BT, Morland AB. 2008. Induced deficits in speed perception by transcranial magnetic stimulation of human cortical areas V5/MT+ and V3A. J Neurosci. 28:6848–6857.

McKeefry DJ, Zeki S. 1997. The position and topography of the human colour centre as revealed by functional magnetic resonance imaging. Brain. 120(Pt 12):2229–2242.

Merriam EP, Gardner JL, Movshon JA, Heeger DJ. 2013. Modulation of visual responses by gaze direction in human visual cortex. J Neurosci. 33:9879–9889.

Murphy AP, Ban H, Welchman AE. 2013. Integration of texture and disparity cues to surface slant in dorsal visual cortex. J Neurophysiol. 110:190–203.

Ogawa S, Takemura H, Horiguchi H, Terao M, Haji T, Pestilli F, Yeatman JD, Tsuneoka H, Wandell BA, Masuda Y. 2014. White matter consequences of retinal receptor and ganglion cell damage. Invest Ophthalmol Vis Sci. 55:6976–6986.

Pajevic S, Pierpaoli C. 1999. Color schemes to represent the orientation of anisotropic tissues from diffusion tensor data: application to white matter fiber tract mapping in the human brain. Magn Reson Med. 42:526–540.

Pestilli F, Yeatman JD, Rokem A, Kay KN, Wandell BA. 2014. Evaluation and statistical inference for human connectomes. Nat Methods. 11:1058–1063.

Press WA, Brewer AA, Dougherty RF, Wade AR, Wandell BA. 2001. Visual areas and spatial summation in human visual cortex. Vision Res. 41:1321–1332.

Reese TG, Heid O, Weisskoff RM, Wedeen VJ. 2003. Reduction of eddy-current-induced distortion in diffusion MRI using a twice-refocused spin echo. Magn Reson Med. 49:177–182.

Rokem A, Yeatman JD, Pestilli F, Kay KN, Mezer A, van der Walt S, Wandell BA. 2015. Evaluating the accuracy of diffusion MRI models in white matter. PLoS ONE. in press.

Rokers B, Cormack LK, Huk AC. 2009. Disparity- and velocity-based signals for three-dimensional motion perception in human MT+. Nat Neurosci. 12:1050–1055.

Saber GT, Pestilli F, Curtis CE. 2015. Saccade planning evokes topographically specific activity in the dorsal and ventral streams. J Neurosci. 35:245–252.

Schluppeck D, Glimcher P, Heeger DJ. 2005. Topographic organization for delayed saccades in human posterior parietal cortex. J Neurophysiol. 94:1372–1384.

Sereno MI, Dale AM, Reppas JB, Kwong KK, Belliveau JW, Brady TJ, Rosen BR, Tootell RB. 1995. Borders of multiple visual areas in humans revealed by functional magnetic resonance imaging. Science. 268:889–893.

Silson EH, McKeefry DJ, Rodgers J, Gouws AD, Hymers M, Morland AB. 2013. Specialized and independent processing of orientation and shape in visual field maps LO1 and LO2. Nat Neurosci. 16:267–269.

Silver MA, Kastner S. 2009. Topographic maps in human frontal and parietal cortex. Trends Cogn Sci. 13:488–495.

Silver MA, Ress D, Heeger DJ. 2005. Topographic maps of visual spatial attention in human parietal cortex. J Neurophysiol. 94:1358–1371.

Smith AT, Greenlee MW, Singh KD, Kraemer FM, Hennig J. 1998. The processing of first- and second-order motion in human visual cortex assessed by functional magnetic resonance imaging (fMRI). J Neurosci. 18:3816–3830.

Sporns O, Tononi G, Kotter R. 2005. The human connectome: a structural description of the human brain. PLoS Comp Biol. 1:e42.

Swisher JD, Halko MA, Merabet LB, McMains SA, Somers DC. 2007. Visual topography of human intraparietal sulcus. J Neurosci. 27:5326–5337.

Tavor I, Yablonski M, Mezer A, Rom S, Assaf Y, Yovel G. 2014. Separate parts of occipito-temporal white matter fibers are associated with recognition of faces and places. NeuroImage. 86:123–130.

Thiebaut de Schotten M, Dell'Acqua F, Forkel SJ, Simmons A, Vergani F, Murphy DG, Catani M. 2011. A lateralized brain network for visuospatial attention. Nat Neurosci. 14:1245–1246.

Thomas C, Avidan G, Humphreys K, Jung KJ, Gao F, Behrmann M. 2009. Reduced structural connectivity in ventral visual cortex in congenital prosopagnosia. Nat Neurosci. 12:29–31.

Thomason ME, Thompson PM. 2011. Diffusion imaging, white matter, and psychopathology. Annu Rev Clin Psychol. 7:63–85.

Tolias AS, Keliris GA, Smirnakis SM, Logothetis NK. 2005. Neurons in macaque area V4 acquire directional tuning after adaptation to motion stimuli. Nat Neurosci. 8:591–593.

Tootell RB, Hadjikhani N, Hall EK, Marrett S, Vanduffel W, Vaughan JT, Dale AM. 1998. The retinotopy of visual spatial attention. Neuron. 21:1409–1422.

Tootell RB, Mendola JD, Hadjikhani NK, Ledden PJ, Liu AK, Reppas JB, Sereno MI, Dale AM. 1997. Functional analysis of V3A and related areas in human visual cortex. J Neurosci. 17:7060–7078.

Tournier JD, Calamante F, Connelly A. 2012. MRtrix: diffusion tractography in crossing fiber regions. Int J Imag Syst Technol. 22:53–66.

Tournier JD, Calamante F, Connelly A. 2007. Robust determination of the fibre orientation distribution in diffusion MRI: non-negativity constrained super-resolved spherical deconvolution. NeuroImage. 35:1459–1472.

Tsao DY, Vanduffel W, Sasaki Y, Fize D, Knutsen TA, Mandeville JB, Wald LL, Dale AM, Rosen BR, Van Essen DC, et al. 2003. Stereopsis activates V3A and caudal intraparietal areas in macaques and humans. Neuron. 39:555–568.

Ungerleider LG, Galkin TW, Desimone R, Gattass R. 2008. Cortical connections of area V4 in the macaque. Cereb Cortex. 18:477–499.

Ungerleider LG, Mishkin M. 1982. Two cortical visual systems. In: Ingle DJ, Goodale MA, Mansfield RJW, editors. The analysis of visual behavior. Cambridge (MA): MIT Press. p. 549–586.

Vanduffel W, Fize D, Mandeville JB, Nelissen K, Van Hecke P, Rosen BR, Tootell RB, Orban GA. 2001. Visual motion processing investigated using contrast agent-enhanced fMRI in awake behaving monkeys. Neuron. 32:565–577.

Van Essen DC, Smith SM, Barch DM, Behrens TE, Yacoub E, Ugurbil K, Consortium WU-MH. 2013. The WU-Minn Human Connectome Project: an overview. NeuroImage. 80:62–79.

Vidyasagar TR, Pammer K. 2010. Dyslexia: a deficit in visuo-spatial attention, not in phonological processing. Trends Cogn Sci. 14:57–63.

Vinberg J, Grill-Spector K. 2008. Representation of shapes, edges, and surfaces across multiple cues in the human visual cortex. J Neurophysiol. 99:1380–1393.

Wade A, Augath M, Logothetis N, Wandell B. 2008. fMRI measurements of color in macaque and human. J Vis. 8(10):6.

Wade AR, Brewer AA, Rieger JW, Wandell BA. 2002. Functional measurements of human ventral occipital cortex: retinotopy and colour. Philos Trans R Soc Lond B Biol Sci. 357:963–973.

Wakana S, Jiang H, Nagae-Poetscher LM, van Zijl PC, Mori S. 2004. Fiber tract-based atlas of human white matter anatomy. Radiology. 230:77–87.

Wandell BA, Dumoulin SO, Brewer AA. 2007. Visual field maps in human cortex. Neuron. 56:366–383.

Wandell BA, Rauschecker AM, Yeatman JD. 2012. Learning to see words. Annu Rev Psychol. 63:31–53.

Wandell BA, Winawer J. 2011. Imaging retinotopic maps in the human brain. Vision Res. 51:718–737.

Wandell BA, Yeatman JD. 2013. Biological development of reading circuits. Curr Opin Neurobiol. 23:261–268.

Wedeen VJ, Rosene DL, Wang R, Dai G, Mortazavi F, Hagmann P, Kaas JH, Tseng WY. 2012. The geometric structure of the brain fiber pathways. Science. 335:1628–1634.

Weiner KS, Grill-Spector K. 2010. Sparsely-distributed organization of face and limb activations in human ventral temporal cortex. NeuroImage. 52:1559–1573.

Wernicke C. 1881. Lehrbuch der Gehirnkrankheiten für Aerzte und Studirende. Kassel: Theodor Fischer.

Winawer J, Horiguchi H, Sayres RA, Amano K, Wandell BA. 2010. Mapping hV4 and ventral occipital cortex: the venous eclipse. J Vis. 10(5):1.

Witthoft N, Nguyen ML, Golarai G, Larocque KF, Liberman A, Smith ME, Grill-Spector K. 2014. Where is human V4? Predicting the location of hV4 and VO1 from cortical folding. Cereb Cortex. 24:2401–2408.

Yeatman JD, Dougherty RF, Ben-Shachar M, Wandell BA. 2012. Development of white matter and reading skills. Proc Natl Acad Sci USA. 109:E3045–E3053.

Yeatman JD, Dougherty RF, Myall NJ, Wandell BA, Feldman HM. 2012. Tract profiles of white matter properties: automating fiber-tract quantification. PLoS ONE. 7:e49790.

Yeatman JD, Rauschecker AM, Wandell BA. 2013. Anatomy of the visual word form area: adjacent cortical circuits and long-range white matter connections. Brain Lang. 125:146–155.

Yeatman JD, Wandell BA, Mezer AA. 2014. Lifespan maturation and degeneration of human brain white matter. Nat Commun. 5:4932.

Yeatman JD, Weiner KS, Pestilli F, Rokem A, Mezer A, Wandell BA. 2014. The vertical occipital fasciculus: a century of controversy resolved by in vivo measurements. Proc Natl Acad Sci USA. 111:E5214–E5223.

Yushkevich PA, Piven J, Hazlett HC, Smith RG, Ho S, Gee JC, Gerig G. 2006. User-guided 3D active contour segmentation of anatomical structures: significantly improved efficiency and reliability. NeuroImage. 31:1116–1128.

Zeki S, Watson JD, Lueck CJ, Friston KJ, Kennard C, Frackowiak RS. 1991. A direct demonstration of functional specialization in human visual cortex. J Neurosci. 11:641–649.

Zhang W, Olivi A, Hertig SJ, van Zijl P, Mori S. 2008. Automated fiber tracking of human brain white matter using diffusion tensor imaging. NeuroImage. 42:771–777.

Supplemental information: A major human white-matter pathway between dorsal and ventral visual cortex

Hiromasa Takemura, Ariel Rokem, Jonathan Winawer, Jason D. Yeatman, Brian A. Wandell, Franco Pestilli
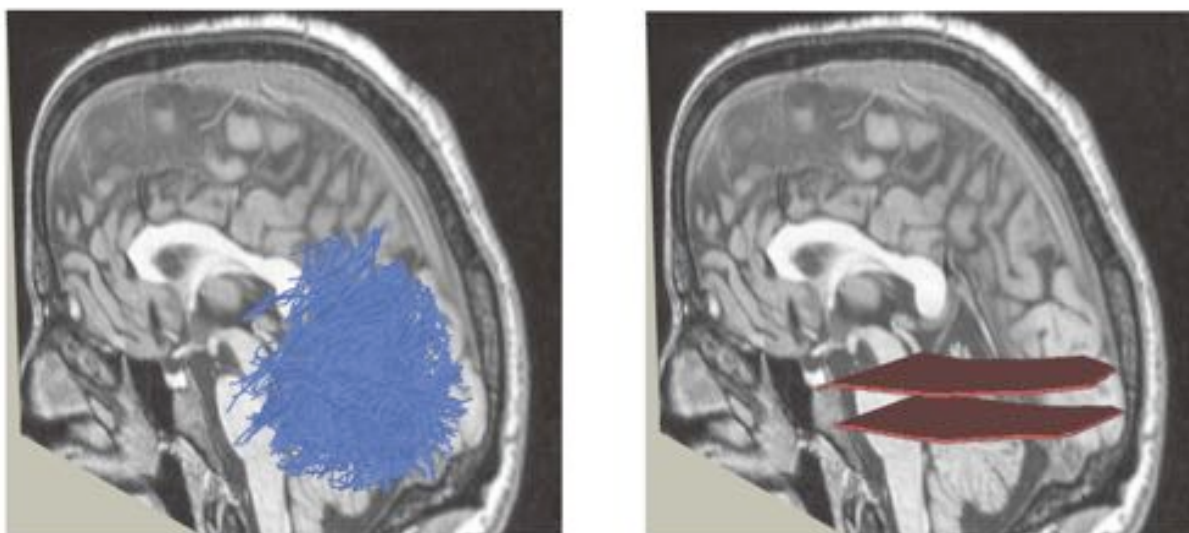
Table of content
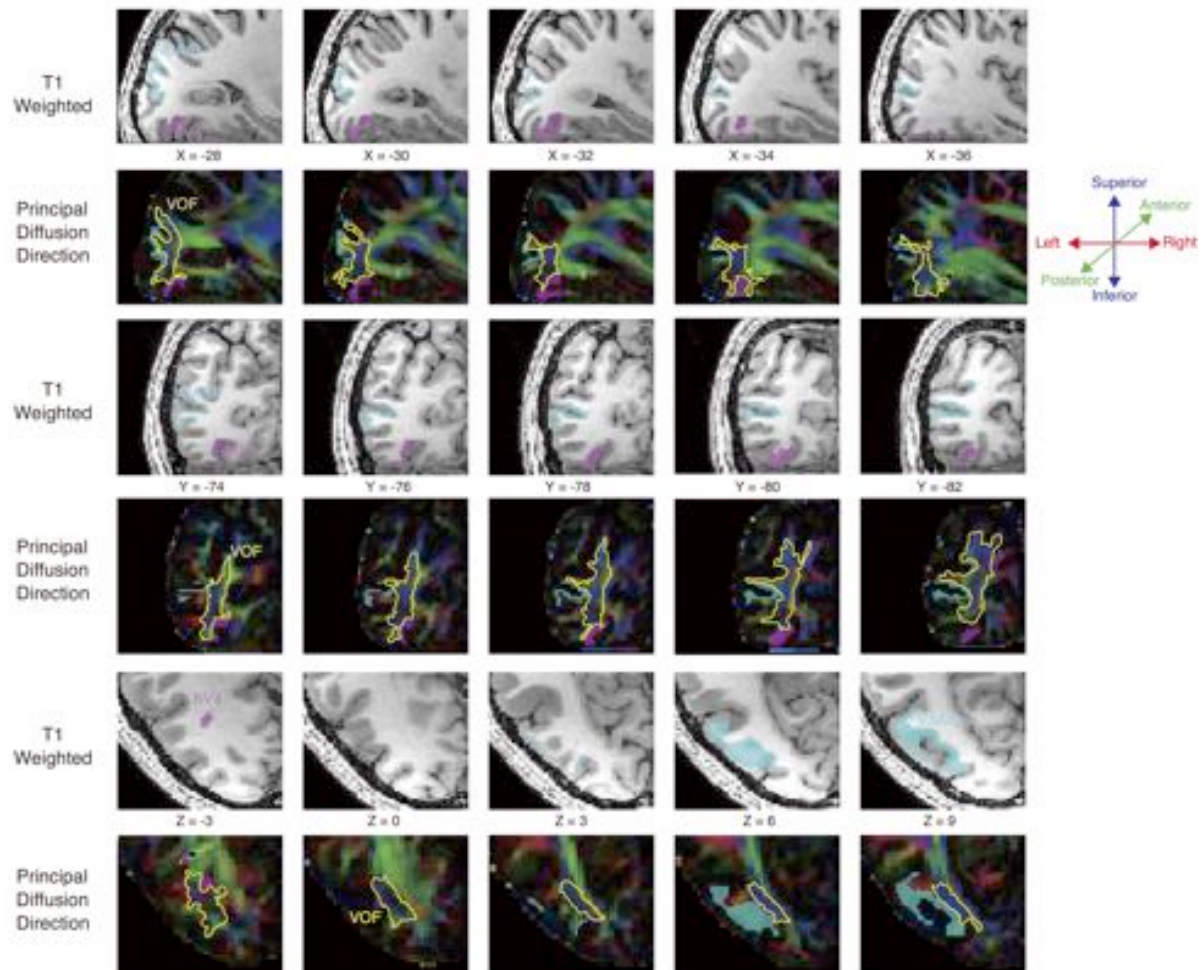
Supplemental Figures

Supplementary Figure 1. VOF segmentation protocol. Left panel; optimized connectome in the occipital white matter generated by LiFE. Right panel: waypoint plane ROIs. The VOF was identified as the set of fascicles in optimized connectome passing through these waypoint plane ROIs.
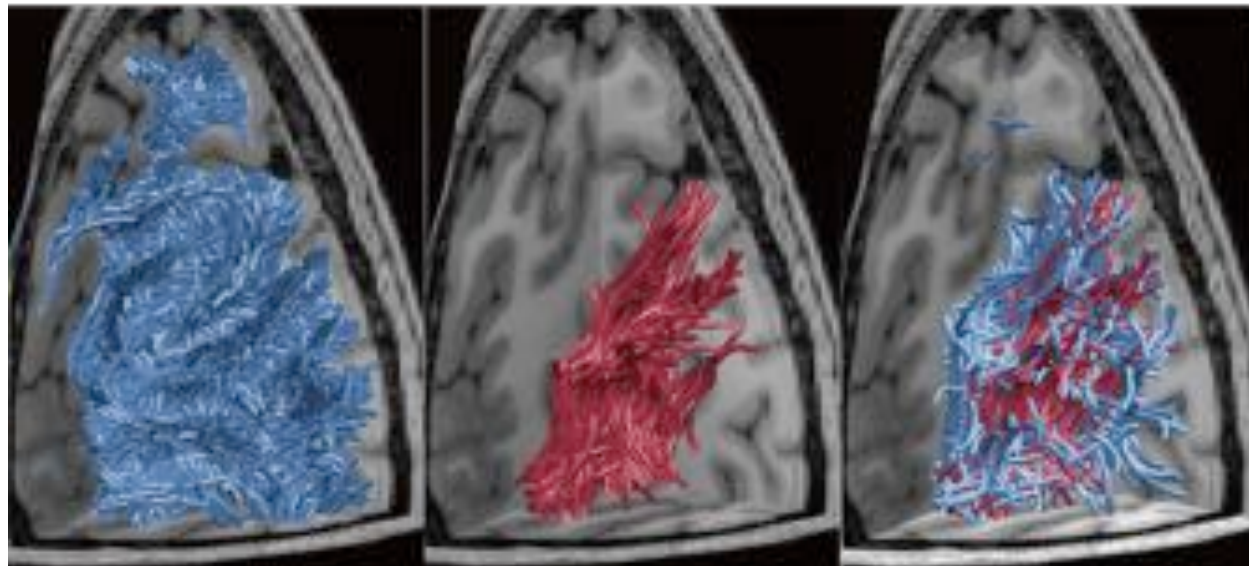
Supplementary Figure 2. Virtual lesion and path-neighborhood. Left panel; example optimal occipital connectome in an individual left-hemisphere (blue). Middle panel; computationally segemented VOF from the optimized connectome in the left panel. Right panel; segmented VOF (red) with the VOF path-neighborhood (blue, only about 10% of the total path-neighborhood fibers are displayed). Figure is reproduced from Pestilli (2015).

VOF and principal diffusion directions

Supplementary Figure 3. VOF and principal diffusion direction map. Slice-by-slice comparison of T1-weighted image and principal diffusion direction map in sagittal (top), coronal (middle) and axial (bottom) section in a representative hemisphere (Subject 1, Left hemisphere). The location of each slice is reported in ACPC coordinate (X, Y and Z). The location of V3A/B (cyan) and hV4 (magenta) are overlaid on both maps. The location of VOF identified by tractography is depicted by the yellow outline. The principal diffusion directions in individual voxels are described by color (red, left-right; green, anterior-posterior; blue, superior-inferior). The principal diffusion direction in the portion of white matter comprising the VOF is oriented predominantly superior-inferior direction (blue).
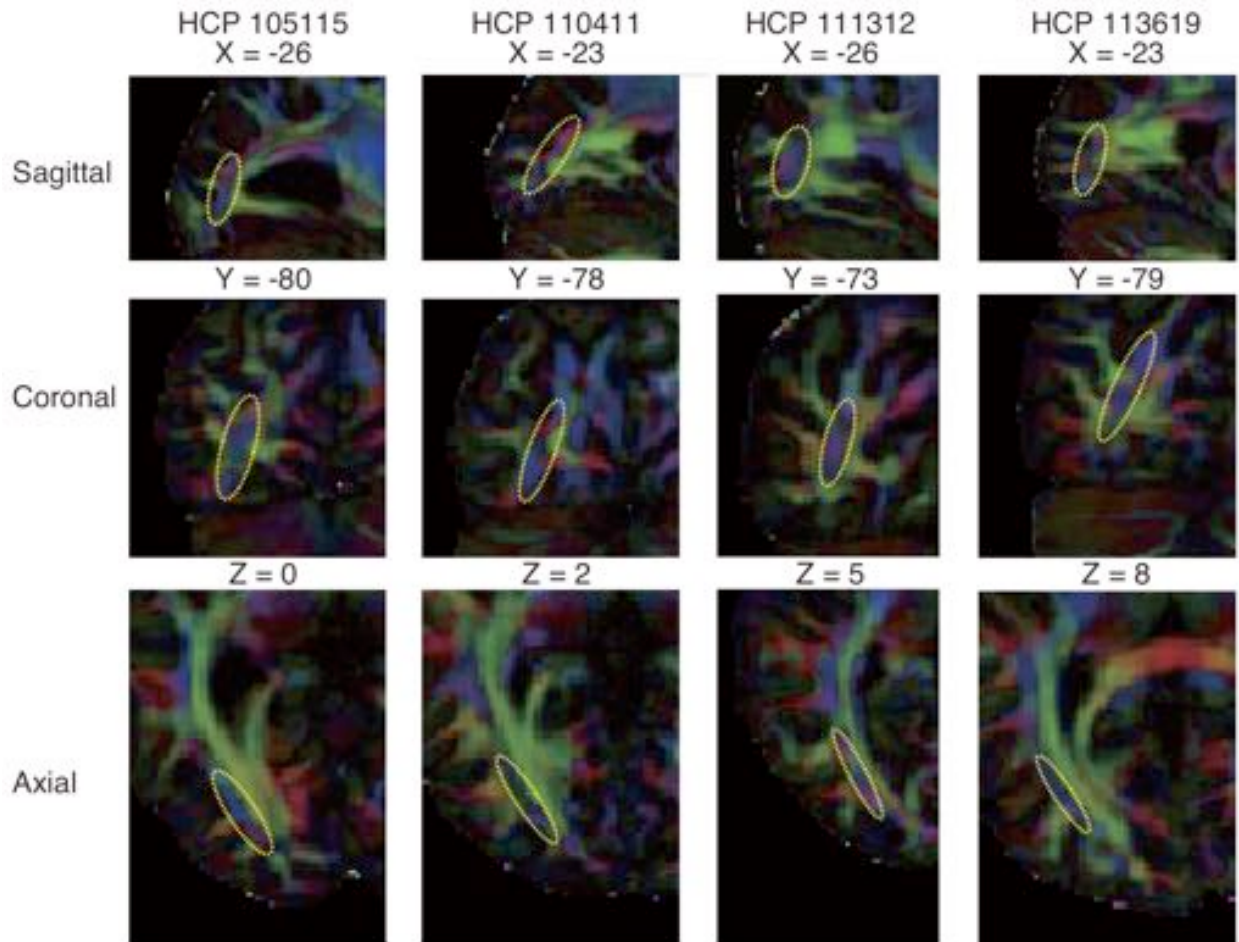
Supplementary Figure 4. VOF and principal diffusion direction map in Human Connectome Project data. Principal diffusion direction map in representative sagittal (top), coronal (middle) and axial (bottom) sections of four individual brains from Human Connectome Project data (left hemisphere). The location of the slice is reported in ACPC coordinates (X, Y and Z). The location of VOF is depicted by the yellow outline. Same conventions as in Supplementary Fig. 3.

Evaluation of connectomes generated by different parameters
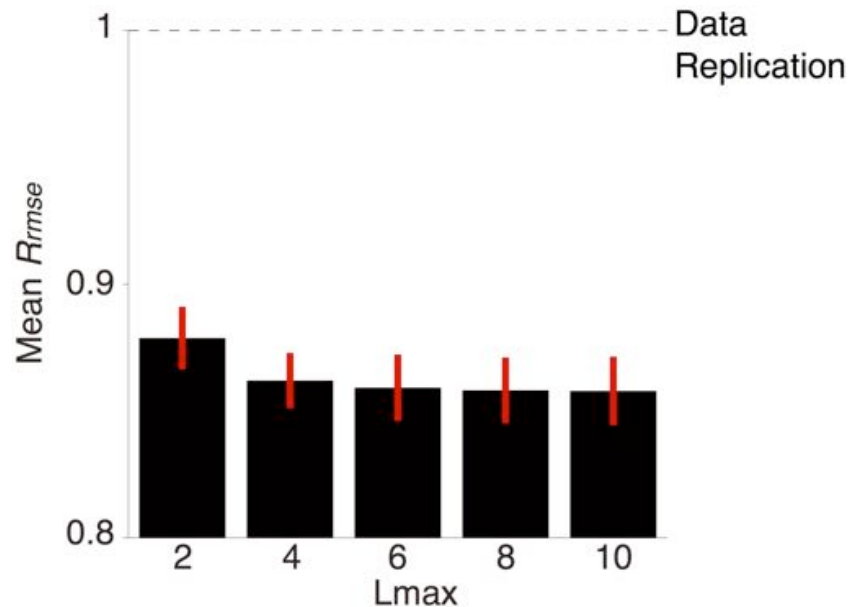
Supplementary Figure 5. Evaluation of connectomes generated by different parameters in CSD models. Vertical axis depicts the prediction accuracy (R_{rmse}, Ratio of RMSE; see Supplementary Experimental Procedure) for diffusion signal by optimized connectomes generated by different parameters in CSD model (L_{max} = 2, 4, 6, 8 and 10). R_{rmse} = 1 means the equivalent prediction accuracy with test-retest reliability. Error bar depicts ±1 s.e.m. across hemispheres. Models show significantly better performance than test-retest reliability (R_{rmse}<1), L_{max} = 2 shows worse performance as compared to the rest of the models.
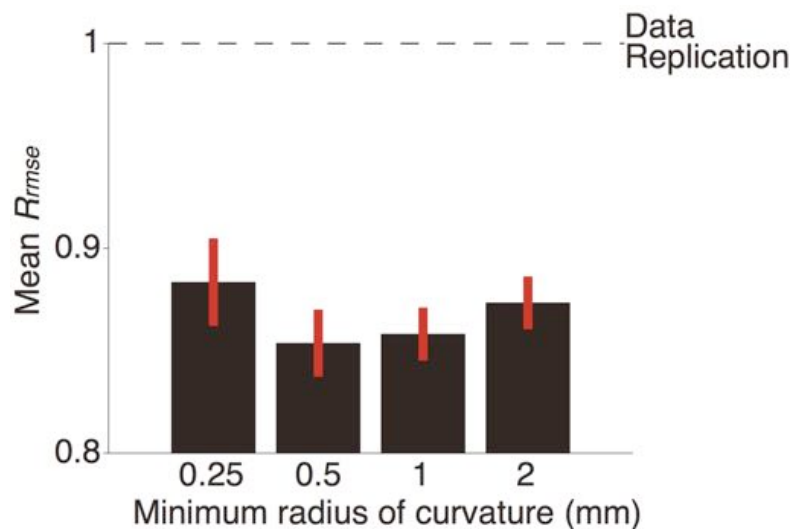

Supplementary Figure 6. Evaluation of connectomes generated using L_{max}=8 with different minimum radius of curvature in fiber tractography. Prediction accuracy for diffusion signal by optimized connectomes generated by different minimum radius of curvature in fiber tractography (0.25, 0.5, 1 and 2mm). Other conventions are identical to those in Supplementary Fig. 5. The models using 0.5 and 1 mm show a better performance.
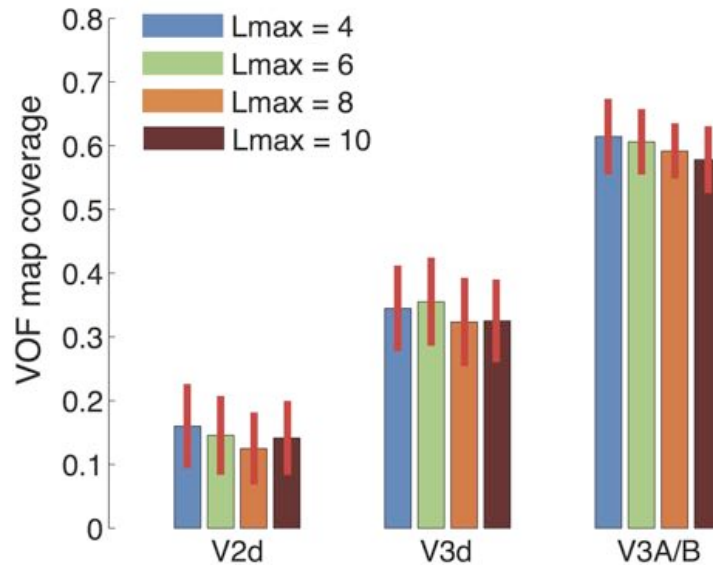
Supplementary Figure 7. Robustness of dorsal VOF projections to the choice of L_{max}.
Vertical axis represents the proportion of voxels in maps within 3 mm from dorsal VOF termination. Color depicts the results in optimized connectomes derived with different CSD model parameters (L_{max} = 4, 6, 8 and 10). Error bar depicts ±1 s.e.m. across 10 hemispheres.
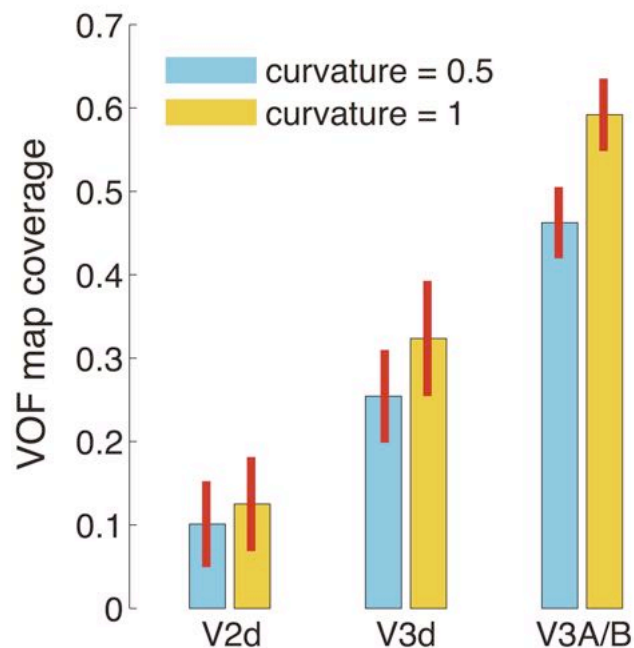

Supplementary Figure 8. Robustness of dorsal VOF projections to the choice of minimum curvature radius for tractography. Vertical axis represents the proportion of voxels in maps within 3 mm from dorsal VOF termination. Each color depicts the results in optimized connectomes from different minimum radius of curvature (0.5 and 1 mm). Error bar depicts ±1 s.e.m. across 10 hemispheres.

Comparison of the statistical evidence between the VOF and major tracts
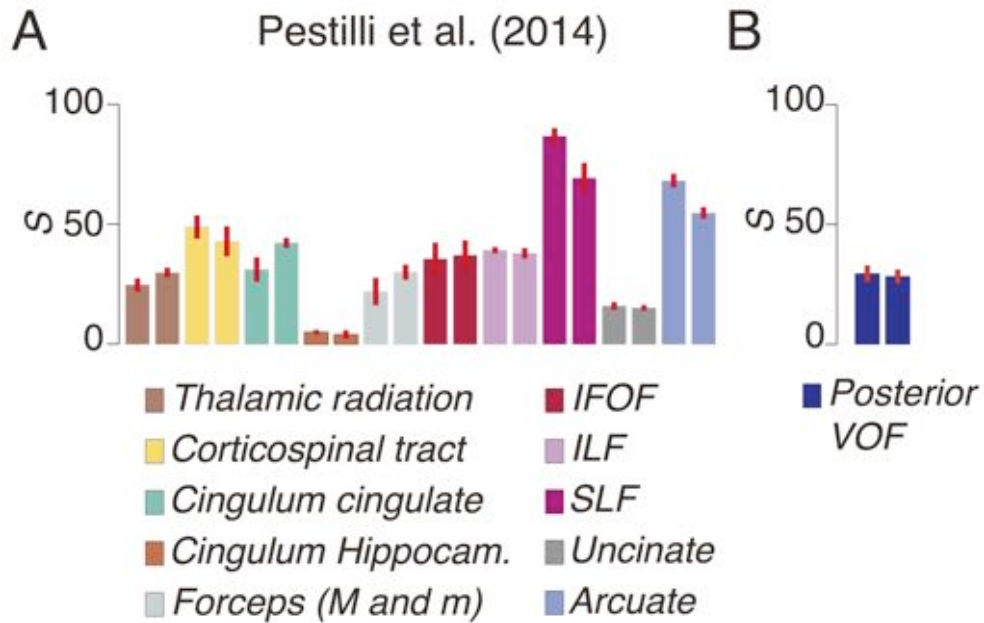
Supplementary Figure 9. Comparison of the strength of evidence between VOF and other tracts. (A) The mean strength of evidence (S) across 5 brains for each of the 20 major tracts. Bar location matches hemisphere (left and right). Reproduced from Pestilli et al. (2014). (B) S across 5 brains for the posterior portion of the VOF identified in this study. Error bar depicts ±1 s.e.m. across brains.
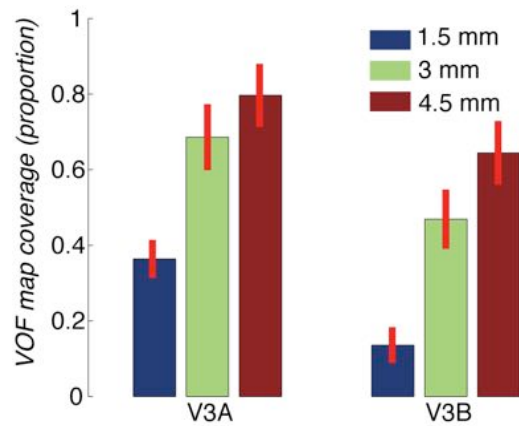
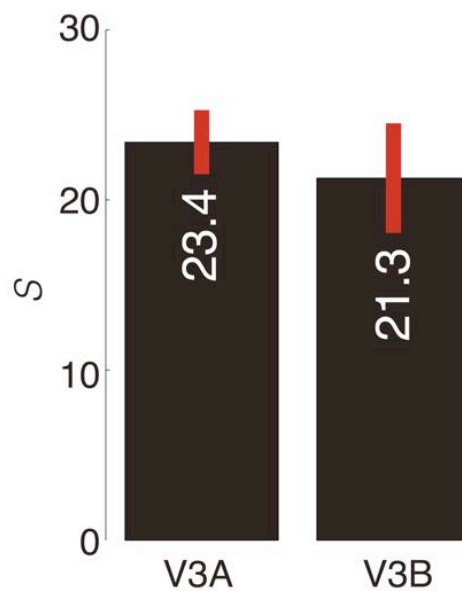*Strength of evidence for the VOF projections to dorsal maps*
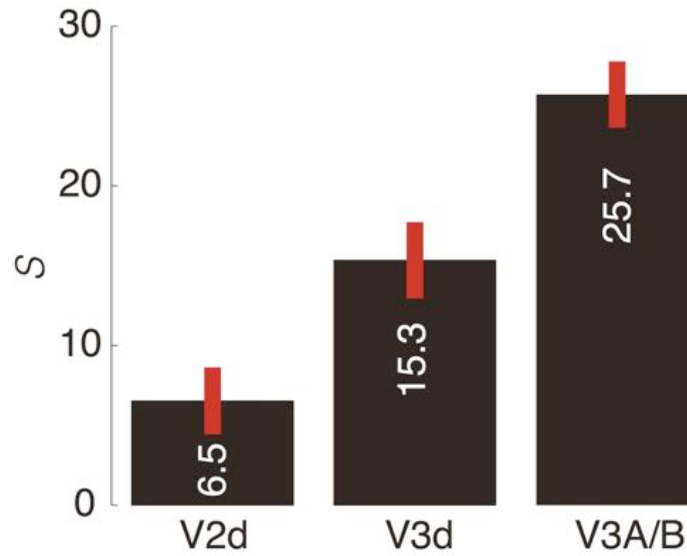
Supplementary Figure 10. Strength of evidence for VOF projections to dorsal maps. Strength of the evidence (*S*) in favor of the portion of VOF projecting V3A/B, V3d and V2d. Error bar depicts ± 1 s.e.m. across occipital lobes (N=10).

VOF projections to V3A and V3B

Supplementary Figure 11. VOF projection to V3A and V3B. VOF map coverage in V3A and V3B in 8 hemispheres, in which the boundary between V3A and V3B can be identified. (We could not distinguish the boundary between V3A and V3B in two hemispheres). Plot conventions follow Figures 3B and 4B.
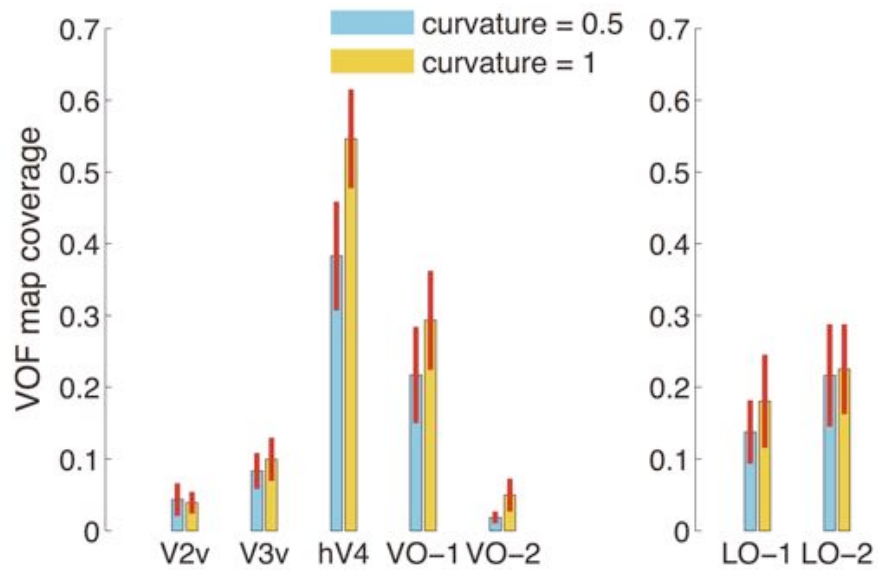

Supplementary Figure 12. Strength of evidence for the VOF projections to V3A and V3B. Strength of the evidence (*S*) in favor of the portion of VOF projecting V3A and V3B in 8 hemispheres (we could not distinguish the boundary between V3A and V3B in two hemispheres). Plot conventions follow Supplementary Fig. 10.
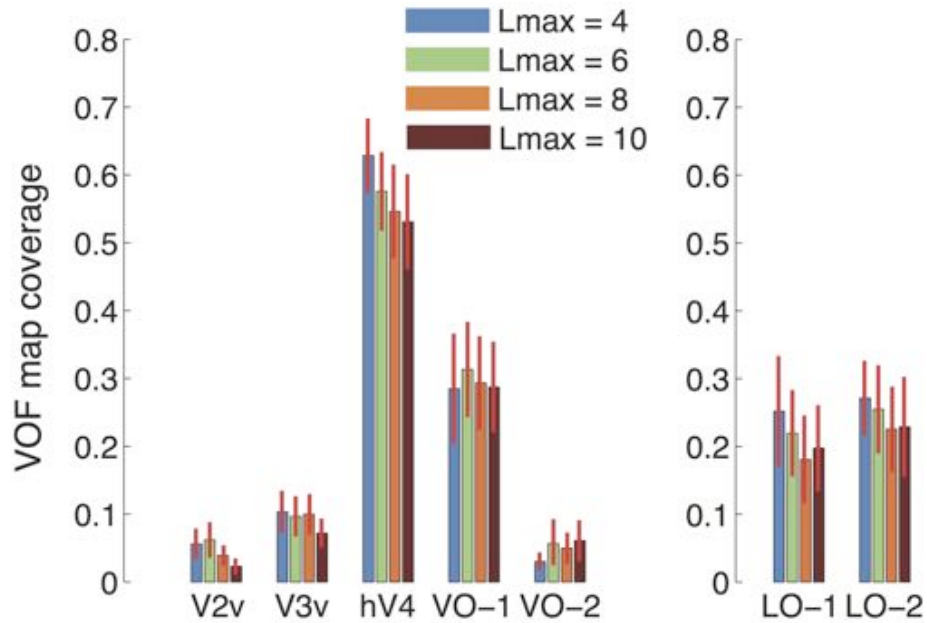
Supplementary Figure 13. Robustness of ventral VOF projections to the choice of L_{max}.
Vertical axis represents the proportion of voxels in the maps within 3 mm from ventral VOF termination. Plot conventions follow Supplementary Fig. 7.
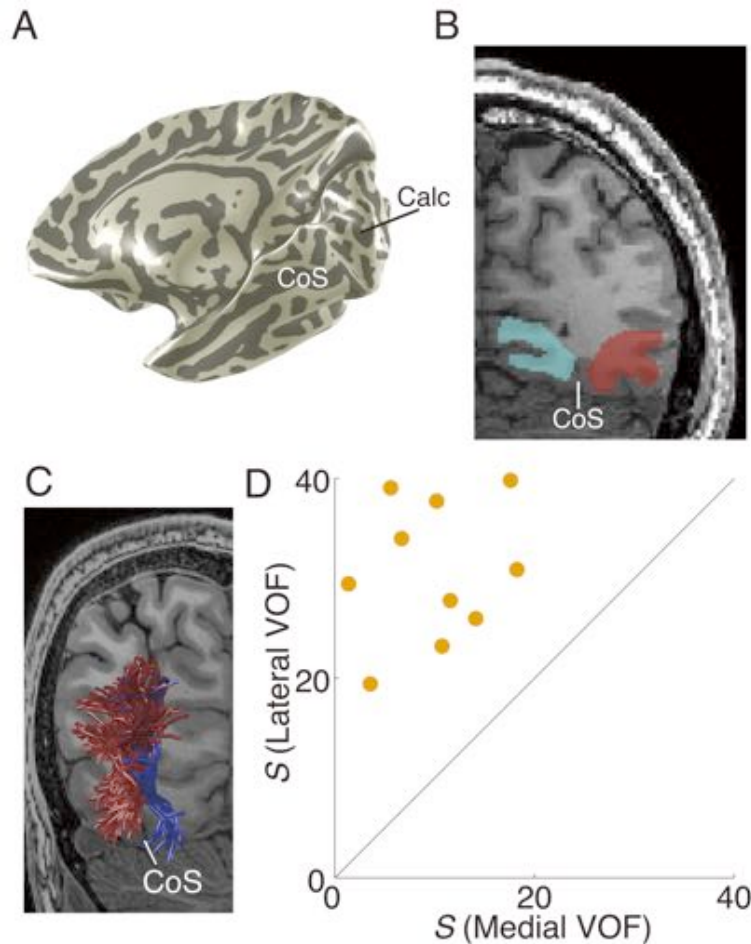

Supplementary Figure 14. Robustness of ventral VOF projections to the choice of the minimum curvature radius. Vertical axis represents the proportion of voxels in maps within 3 mm from ventral VOF termination. Plot conventions follow Supplementary Fig. 8.

Strength of evidence for the VOF projections to ventral and lateral maps
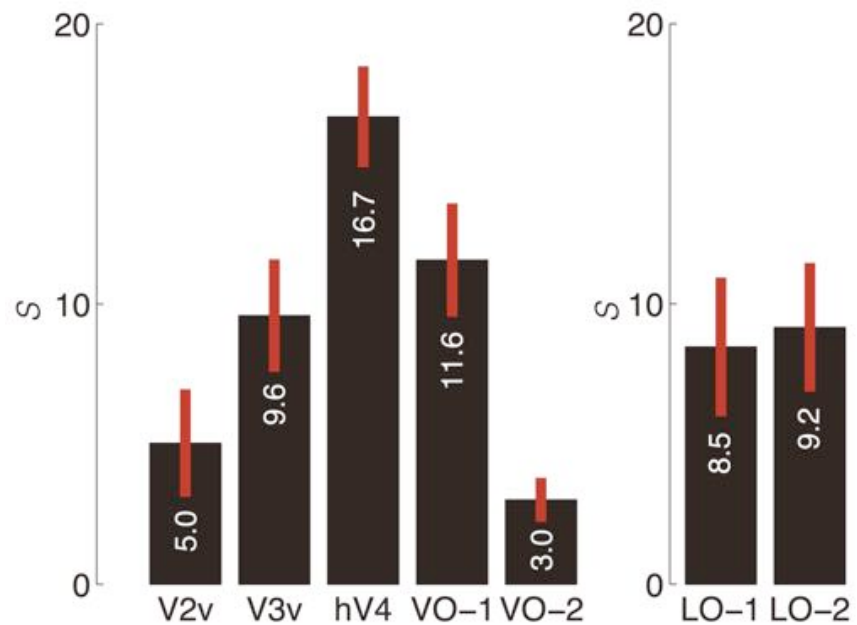
Supplementary Figure 15. Strength of evidence for VOF projections to ventral and lateral maps. Strength of the evidence (*S*) in favor of the portion of VOF projecting ventral (left panel) and lateral maps (right panel). Error bar depicts ± 1 s.e.m. across occipital lobes (N=10).

Supplementary Figure 16. Anatomical identification of the Collateral sulcus and statistical evaluation of the VOF. (A) Anatomical location of Collateral Sulcus (CoS) on smoothed cortical surface (subject 3, right hemisphere). Calc: Calcarine sulcus. (B) Waypoint ROI covering the white matter in lateral (blue) or medial side (red) from CoS. Lateral or Medial VOF is defined as VOF fascicle groups projecting these white matter regions. (C) Example of lateral (red) and medial (blue) VOF fascicles defined in relation to the collateral sulcus (CoS; subject 1, left hemisphere). (D) Strength of the connection evidence (S) for medial (x axis) and lateral VOF fascicles (y axis) in each hemispheres.

Supplemental Methods

Human connectome project data set

We used four brains with DWI data supplied by the Human Connectome Project (Van Essen et al., 2013; https://www.humanconnectome.org/data/). Measurements from the 2000 s/mm^2 shell were extracted from the original data, preprocessed using the same procedure used for the rest of the data presented in the main manuscript (see Materials and Methods). The location of the VOF was identified by looking at the principal diffusion direction map in this higher-resolution dataset (Supplementary Fig. 4).

Evaluation of connectomes generated by different parameters

Fiber tractography includes parameters that are selected by users. LiFE enables evaluating connectomes generated by different parameters (Pestilli et al. 2014). Here, we explain how we evaluated connectomes using different tractogtraphy parameters.

First, we generated candidate connectomes using different parameters (L_{max}=2, 4, 6, 8 and 10; the minimum radius of curvature = 0.25, 0.5, 1 and 2 mm, whereas other parameters were kept). Second for each connectome we generated an optimized connectome using LiFE. Finally, we compared model accuracy of optimized connectomes generated by different parameters.

We compared model accuracy of optimized connectomes by comparing the prediction error, namely the root-mean-squared difference (RMSE) between the diffusion signal measured and the synthetic diffusion signal predicted by the LiFE using the optimized connectome. Model prediction error (M_{rmse}) in a voxel is defined as:

$$M_{rmse} = \sqrt{\frac{\sum_{i=1}^{N}(m(\theta_i) - S_2(\theta_i))^2}{N}}$$
(Eq.S1)

Where $m(\theta_i)$ is the diffusion-modulation predicted by connectome model at each measured diffusion direction θ_i and $S_2(\theta_i)$ is the measured diffusion-modulation signal in a second, independent set of diffusion data not used for tractography. N is a number of measured diffusion directions. M_{rmse} is compared to test-retest reliability (D_{rmse}):

$$D_{rmse} = \sqrt{\frac{\sum_{i=1}^{N}(S_1(\theta_i) - S_2(\theta_i))^2}{N}}$$
(Eq.S2)

Where $S_1(\theta_i)$ and $S_2(\theta_i)$ are the diffusion-modulation measured in two independent data sets, one used for tractography the other not used for tractography. M_{rmse} is normalized by D_{rmse}, to compute the Ratio of Root Mean Square Errors (R_{rmse}):

$$R_{rmse} = \frac{M_{rmse}}{D_{rmse}} \qquad\qquad\qquad \text{(Eq.S3)}$$

R_{rmse} = 1 indicates that the optimized connectome generated form Data 1 predicts Data 2 as well as Data 1 predicts Data 2 (test-retest reliability). We use R_{rmse} to compare optimized connectomes generated by different tractography parameters (Supplementary Fig. 5 and 6).

Supplementary Fig. 5 compares model accuracy within the voxels of the VOF across connectomes generated by different parameters of CSD models (L_{max} = 2, 4, 6, 8 and 10). Connectomes generated by L_{max} = 2 show significantly worse R_{rmse}, whereas R_{rmse} does not significantly differ across all other connectomes (L_{max} = 4, 6, 8 and 10). Within the optimal parameter range (L_{max} = 4, 6, 8 and 10), the cortical projection pattern of the VOF is very similar across parameters (Supplementary Fig. 7 and 13). Selection of this parameter from the optimal range does not affect the main conclusion of the study.

Supplementary Fig. 6 compares connectomes generated with a range of the minimum radius of curvature for fiber tracking (Tournier et al. 2012). Connectomes generated using 0.25 and 2 mm minimum radius of curvature showed worse performance. R_{rmse} was comparable between model using 0.5 and 1 mm curvature radius. We consistently observed the VOF projections to V3A/B and hV4 in connectome model using both 0.5 and 1 mm (Supplementary Fig. 8 and 14). Selection of curvature parameters from the optimal range does not affect the conclusions of the study.

References

Pestilli F. 2015. Test-retest measurements and digital validation for in vivo neuroscience. Scientific Data 2:140057.
Pestilli F, Yeatman JD, Rokem A, Kay KN, Wandell BA. 2014. Evaluation and statistical inference for human connectomes. Nat Methods 11:1058-1063.
Tournier JD, Calamante F, Connelly A. 2012. MRtrix: Diffusion tractography in crossing fiber regions. International Journal of Imaging Systems and Technology. 22:53-66.
Van Essen DC, Smith SM, Barch DM, Behrens TE, Yacoub E, Ugurbil K, Consortium WU-MH. 2013. The WU-Minn Human Connectome Project: an overview. NeuroImage. 80:62-79.